Comput Mech (2014) 54:973–986
DOI 10.1007/s00466-014-1046-9

ORIGINAL PAPER

Space–time fluid mechanics computation of heart valve models

Kenji Takizawa · Tayfun E. Tezduyar · Austin Buscher · Shohei Asada

Received: 24 May 2014 / Accepted: 9 June 2014 / Published online: 11 July 2014

Abstract Fluid mechanics computation of heart valves with an interface-tracking (moving-mesh) method was one of the classes of computations targeted in introducing the space–time (ST) interface tracking method with topology change (ST-TC). The ST-TC method is a new version of the Deforming-Spatial-Domain/Stabilized ST (DSD/SST) method. It can deal with an actual contact between solid surfaces in flow problems with moving interfaces, while still possessing the desirable features of interface-tracking methods, such as better resolution of the boundary layers. The DSD/SST method with effective mesh update can already handle moving-interface problems when the solid surfaces are in near contact or create near TC, if the "nearness" is sufficiently "near" for the purpose of solving the problem. That, however, is not the case in fluid mechanics of heart valves, as the solid surfaces need to be brought into an actual contact when the flow has to be completely blocked. Here we extend the ST-TC method to 3D fluid mechanics computation of heart valve models. We present computations for two models: an aortic valve with coronary arteries and a mechanical aortic valve. These computations demonstrate that the ST-TC method can bring interface-tracking accuracy to fluid mechanics of heart valves, and can do that with computational practicality.

K. Takizawa · S. Asada
Department of Modern Mechanical Engineering and Waseda Institute for Advanced Study, Waseda University, 1-6-1 Nishi-Waseda, Shinjuku-ku, Tokyo 169-8050, Japan
e-mail: Kenji.Takizawa@tafsm.org

T. E. Tezduyar (✉) · A. Buscher
Mechanical Engineering, Rice University, MS 321, 6100 Main Street, Houston, TX 77005, USA
e-mail: tezduyar@tafsm.org

Keywords Heart valves · Fluid mechanics computation · Contact · Topology change · Space–time interface-tracking · ST-TC method · DSD/SST method · Moving-mesh method

1 Introduction

The space–time (ST) interface-tracking method with topology change (ST-TC) was introduced in [1]. This is an interface-tracking (moving-mesh) method that can deal with an actual contact between solid surfaces or other TC in flow problems with moving interfaces. It possesses the desirable features of interface-tracking methods that do not come easily or do not come at all with the interface-capturing (nonmoving-mesh) methods. These desirable features include mass conservation across the interface and better resolution of the boundary layers. Comments on relative features of interface-tracking and interface-capturing methods can be found in [1], and also in [2–4]. Fluid mechanics computation of heart valves with an interface-tracking method was one of the classes of problems targeted in introducing the ST-TC method. Accurate calculation of the wall shear stress (WSS) in cardiovascular fluid mechanics computations requires good resolution of the boundary layers (see [5–8]).

The ST-TC method is a new version of the Deforming-Spatial-Domain/Stabilized ST (DSD/SST) method, which was introduced in [9–11] and has been evolving [2,4,12–14]. The DSD/SST method is an alternative to the Arbitrary Lagrangian–Eulerian (ALE) finite element formulation [15], which is the most widely used moving-mesh technique, with many applications and much progress in fluid–structure interaction (FSI) (see, for example, [4,16–53]). Comments on and examples for what the DSD/SST method brings to the table beyond what the ALE method does can be found in [1], and

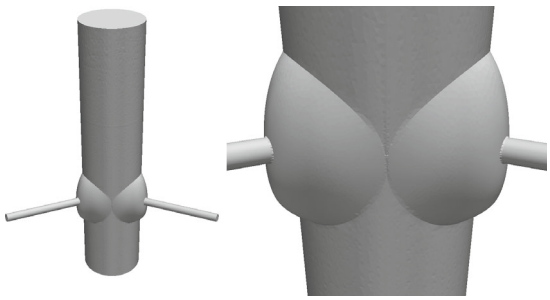

Fig. 1 Aortic valve with coronary arteries. Model geometry. Aorta, leaflets, sinuses, and coronary arteries. The left coronary artery is on the *right* in the figure, and the right coronary artery is on the *left*

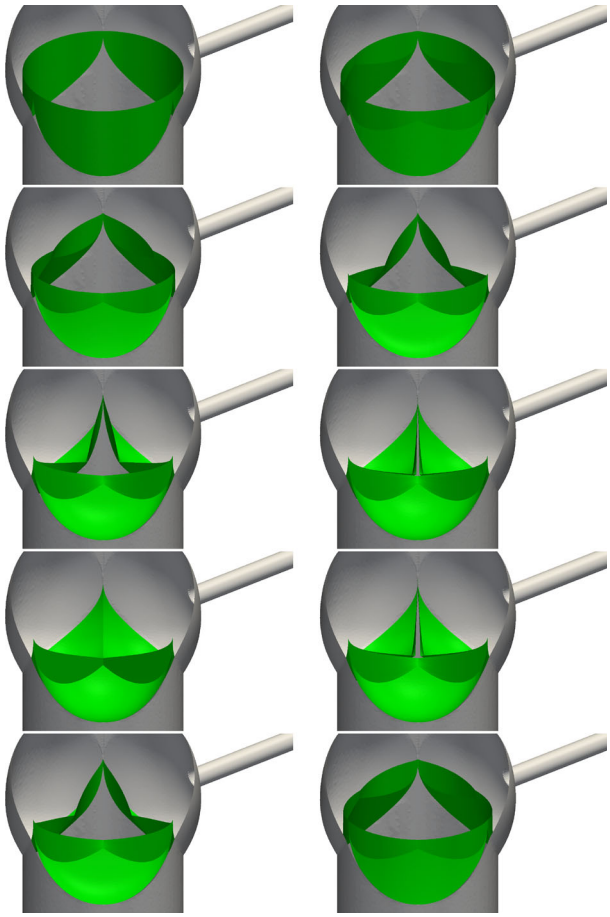

Fig. 2 Aortic valve with coronary arteries. Leaflets at $t/T = 0.0, 0.1, 0.2, 0.3, 0.4, 0.5, 0.6, 0.7, 0.8$ and 0.9 (*left* to *right* and then *top* to *bottom*)

also in [4,13,14,54–58], including examples from aerodynamics of flapping wings and wind turbines.

As commented in [1], the DSD/SST method, when supplemented with robust mesh update, has been proven effective even in handling moving-interface problems when the solid surfaces are in near contact or create near TC, if the "nearness" is sufficiently "near" for the purpose of solving the problem. Examples of that from earlier computations were referenced in [1]. However, as also commented in [1], in some

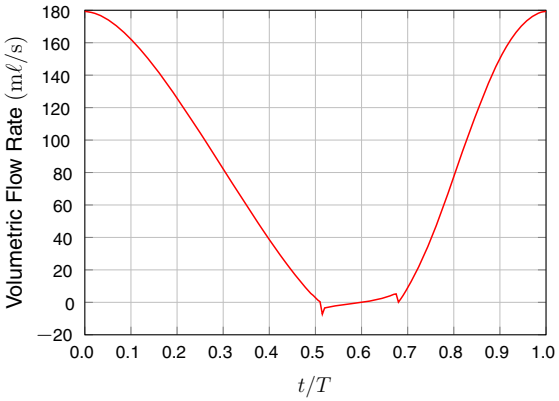

Fig. 3 Aortic valve with coronary arteries. Inflow profile

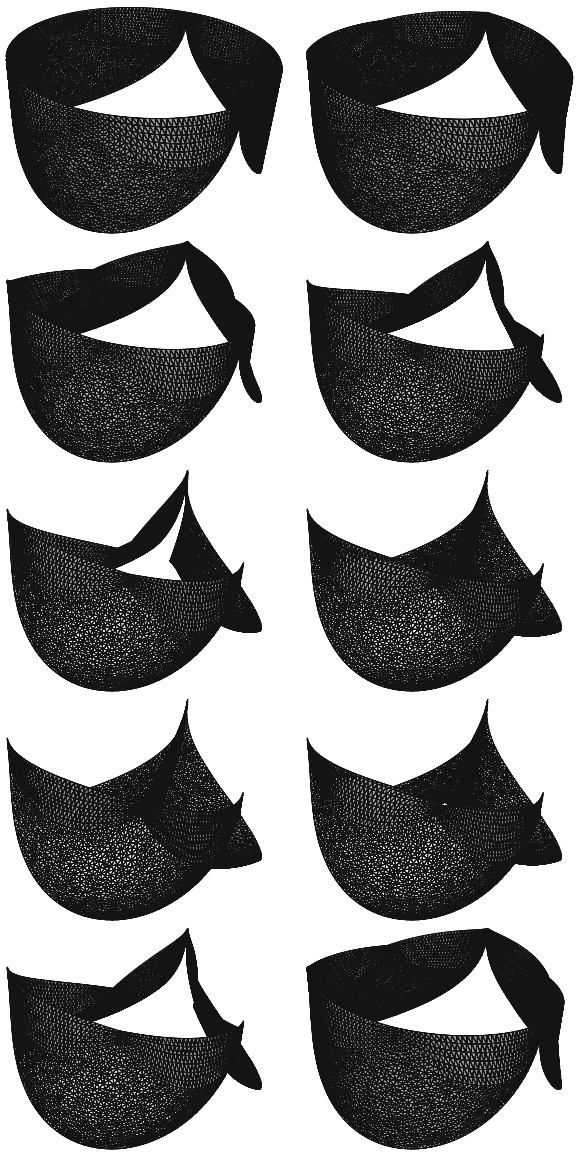

Fig. 4 Aortic valve with coronary arteries. The leaflets surface mesh at the same instants as in Fig. 2

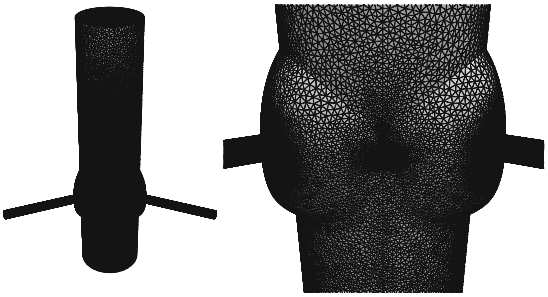

Fig. 5 Aortic valve with coronary arteries. Mesh of the aortic valve, sinuses and coronary arteries

moving-interface problems with contact between the solid surfaces, the "nearness" that can be modeled with a moving-mesh method without actually bringing the surfaces into contact might not be "near" enough for the purpose of solving the problem. Fluid mechanics of heart valves, where the flow has to be completely blocked when the valve is closed, was mentioned in [1] as an example of that. It was also mentioned in [1] that Fluid–Solid Interface-Tracking/Interface-Capturing Technique (FSITICT) [59] was motivated by such cardiovascular FSI problems. In the FSITICT, we track the interface we can with a moving mesh, and capture over that moving mesh the interfaces we cannot track, specifically the interfaces where we need to have an actual contact between the solid surfaces. Essentially, the FSITICT is based on giving up on the interface-tracking accuracy in the parts of the domain where we expect an actual contact. While this is better than giving up on the interface-tracking accuracy everywhere in the domain by using purely an interface-capturing method, the flow would not be represented accurately between the solid surfaces as they close.

The ST-TC method does not give up on interface-tracking accuracy even where there is an actual contact between solid surfaces or other TC. It is a practical alternative to using unstructured ST meshes. Details of the ST-TC method can be found in [1], together with conceptual examples and 2D test computations with models representative of the classes of problems targeted with the method. In this paper, which is in essence a continuation of [1], we extend the ST-TC method to 3D fluid mechanics computation of heart valve models. We consider two models: an aortic valve with coronary arteries and a mechanical aortic valve. We present the computations for the aortic valve with coronary arteries in Sect. 2, and for the mechanical aortic valve in Sect. 3. The concluding remarks are given Sect. 4.

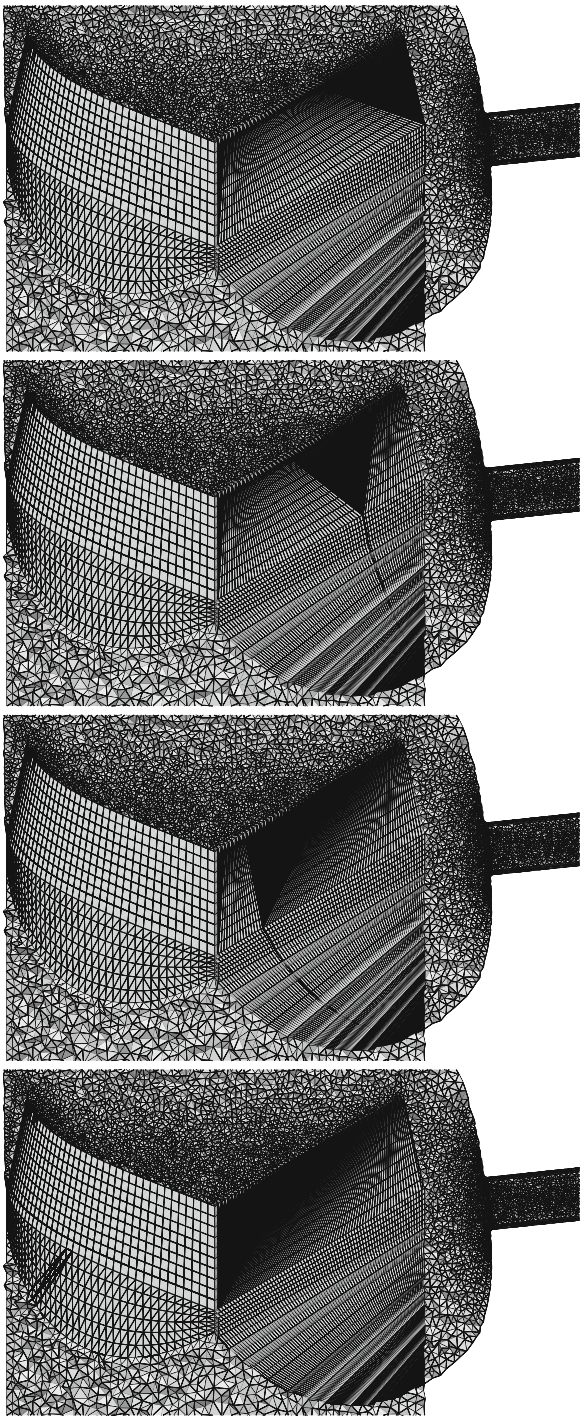

Fig. 6 Aortic valve with coronary arteries. Mesh around the leaflets at $t/T = 0.0$, 0.2, 0.4 and 0.6

2 Aortic valve with coronary arteries

2.1 Geometry and motion modeling

We create a typical aortic-valve model based on pictures, such as the one in [60]. The model, shown in Figs. 1 and 2, has three leaflets with two outlets, corresponding to coronary arteries, and one main outlet, corresponding to the beginning of the aorta. The outlets are extended straight in each direction. The bulges are called sinuses. The left and right coronary arteries are attached to the left and right aortic sinuses, respectively, and the other sinus is called the posterior aortic sinus. The

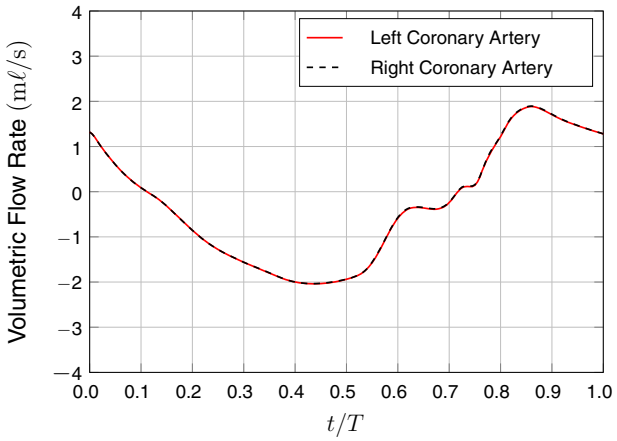

Fig. 7 Aortic valve with coronary arteries. Flow rate at the outlets of the coronary arteries

inlet and main outlet diameters are 23 mm, which correspond to a typical aorta. The two coronary artery diameters are 2.9 mm.

We prescribe the motion of the three leaflets so that the valve closes and opens with a period of $T = 0.6$ s. The motion of the leaflets can be seen in Fig. 2. The valve closes in 0.30 s, tightens for 0.06 s, loosens (while still closed) for 0.04 s, and opens in 0.20 s. This time profile is similar to how it is for an actual valve. The inflow velocity is specified such that the average flow rate is 5,000 mℓ/min. The flow rate is a time-variant function of the horizontal projection of the open mouth area of the valve when it is open, and of the inlet-side volume change while the valve is changing shape after it closes (see Fig. 3). The density and kinematic viscosity of the blood are 1,000 kg/m^3 and 4.0×10^{-6} m^2/s.

The boundary conditions are no-slip on the arterial walls and valves, traction-free at the outflow boundaries, and uniform velocity at the inflow boundary. The surface mesh on the leaflets (shown in Fig. 4) is made of 8,448 nodes and 16,440 triangular faces. The arterial-wall surface mesh is shown in Fig. 5. The mesh has structured, inner zones around the leaflets and an unstructured, outer zone. The inner zones consist of tetrahedral, pyramid-shaped and wedge-shaped elements, and the outer zone consists of tetrahedral elements. The volume mesh is made of 1,417,910 nodes and 4,184,614 elements. The mesh near the valve is shown in Fig. 6.

During the prescribed motion, only the inner zones move with a special, algebraic mesh-moving technique. The positions of the nodes in the inner zones are created by linearly interpolating the surface mesh of the zones from the closed position to the open position. We have 79 layers of nodes extruded from both the upper and lower surfaces of the leaflets.

When the valve is completely open, all of the nodes extruded from the upper surface are slaves to the upper surface, and all of the nodes extruded from the lower surface

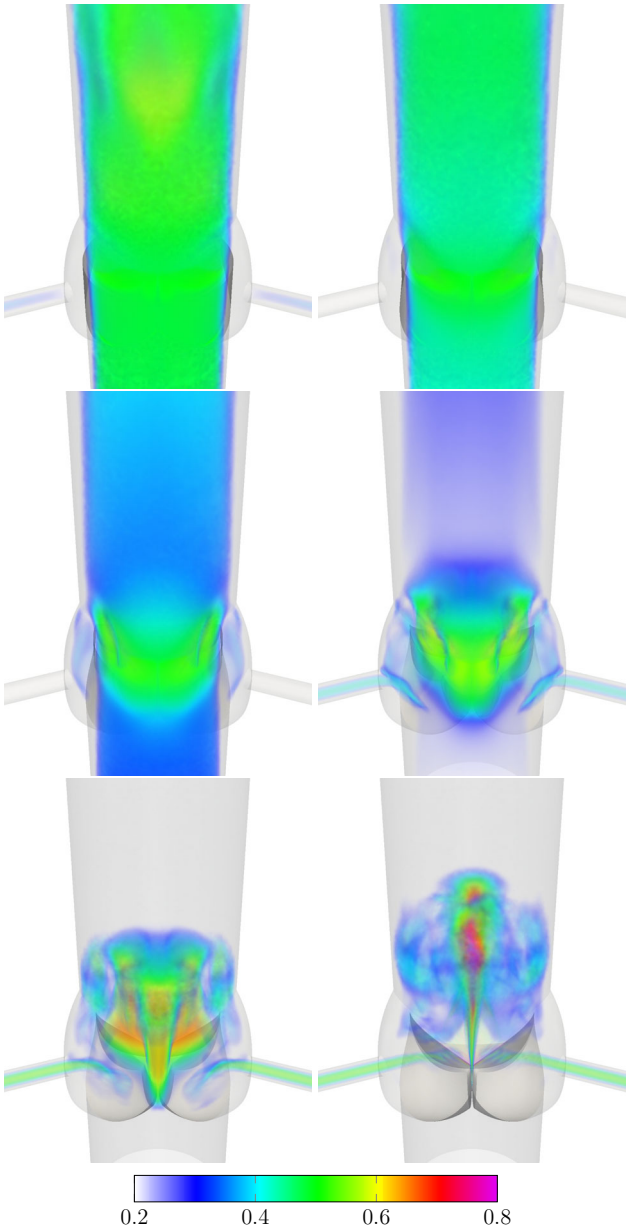

Fig. 8 Aortic valve with coronary arteries. Volume rendering of the velocity magnitude (m/s) at $t/T = 0.0$, 0.1, 0.2, 0.3, 0.4 and 0.5

are masters. As the valve closes, it leaves one layer of nodes attached to the upper surface behind, and the leaflet surface moves to the next node position, making those nodes slaves to the lower surface. When the valve is completely closed, all of the nodes extruded from the upper surface are masters and all of the nodes extruded from the lower surface are slaves to the lower surface.

2.2 Computational conditions

We use the DSD/SST-SUPS and DSD/SST-VMST (convective) techniques for the first two and last two nonlinear iterations of each time step, respectively. The stabilization para-

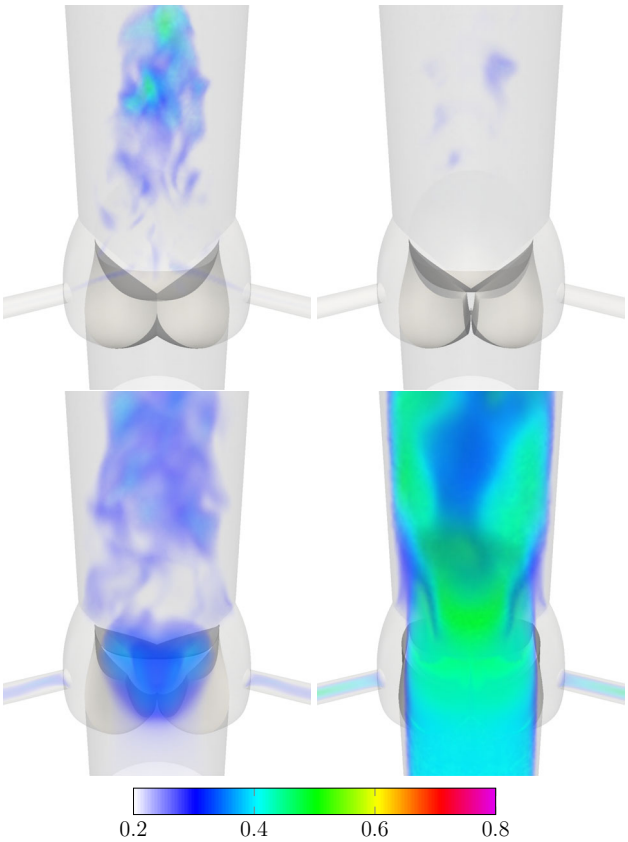

Fig. 9 Aortic valve with coronary arteries. Volume rendering of the velocity magnitude (m/s) at $t/T = 0.6, 0.7, 0.8$ and 0.9

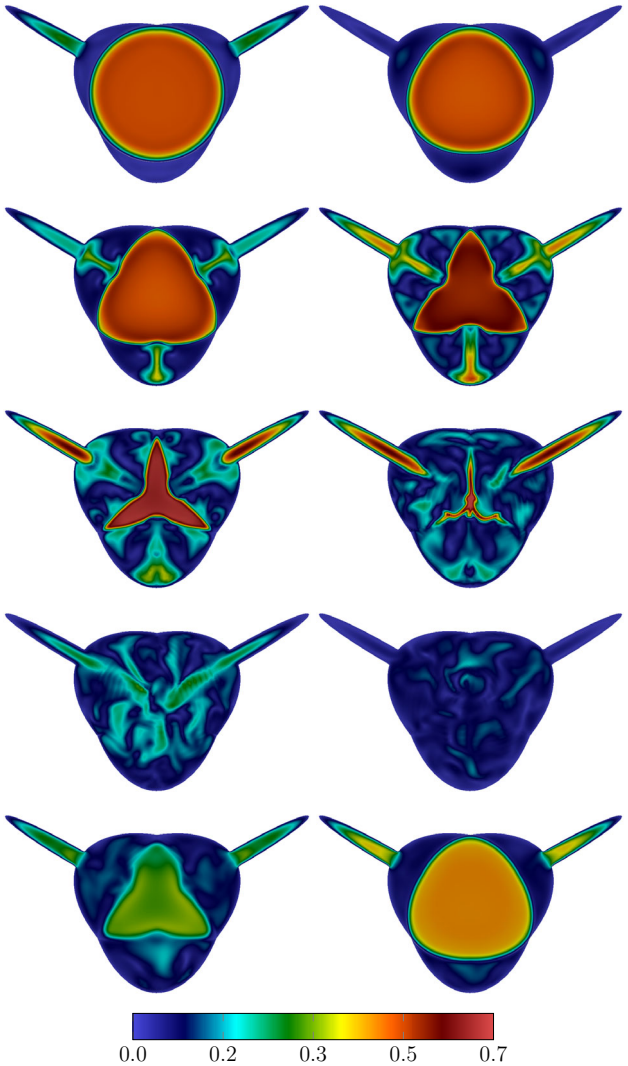

Fig. 10 Aortic valve with coronary arteries. The velocity magnitude (m/s) on the coronary plane at the same instants as in Fig. 2

meter τ_{SUPS} comes from the τ_{SUPG} definition in [2], specifically the definition given by Eqs. (107)–(109) in [2], which can also be found as the definition given by Eqs. (7)–(9) in [12], with ν_{LSIC} from Eq. (17) in [12]. Prior to the prescribed motion, we compute 150 time steps with the geometry at $t = 0$ to develop the flow field. The viscosity of 4.0×10^{-6} m^2/s is reached by ramping over the first 50 time steps starting from the viscosity 1.31×10^{-3} m^2/s. The ramping profile for the viscosity is designed to result in a linear ramping for the Reynolds number. The time-step size is 6.33×10^{-3} s during flow-field development, and 3.00×10^{-3} s for the prescribed-motion cycles. In computing the developed-flow field, the number of GMRES iterations per nonlinear iteration is 150, 350, 450 and 800. In computing the flapping cycles, the number of GMRES iterations is 250, 500, 750 and 1,000. We compute two cycles and display the results for the second cycle.

2.3 Results

The global mass-balance error, normalized by the average flow rate, is less than 10%. Figure 7 shows the flow rate at the outlets of the coronary arteries. There is some "negative outflow" (i.e. inflow) from the coronary arteries, however, the WSS on the long pipes is large enough to stabilize the overall system. Figures 8 and 9 show a volume rendering of the velocity magnitude. Nonsymmetric and complex flow patterns are observed behind the valve. Figures 10 and 11 show the velocity magnitude on the "coronary plane," where the coronary arteries are connected to the aorta, and the "above-sinus plane," which is 18 mm downstream from the coronary plane. The mainstream flow oscillates away from the sinuses. This is mainly due to the jet from the contact of the leaflets of the sinuses.

Figure 12 shows the pressure difference between the lower and upper surfaces of the leaflets. We exclude the parts where the leaflets are in contact. Figures 13 and 14 show the WSS on the leaflet surfaces. The WSS on the lower surfaces of the three leaflets are somewhat similar to each other. However,

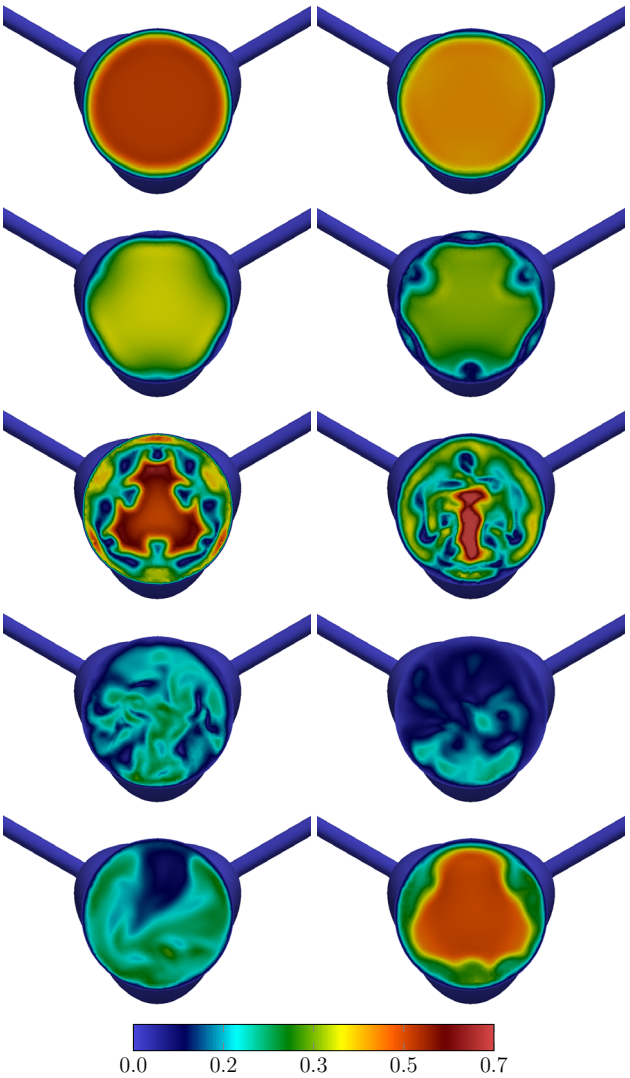

Fig. 11 Aortic valve with coronary arteries. The velocity magnitude (m/s) on the above-sinus plane at the same instants as in Fig. 2

on the upper surfaces, the WSS for the leaflets of the coronary sinuses are different from the WSS for the leaflet of the posterior sinus. Figure 15 shows the OSI on the leaflet surfaces. The WSS vector is projected onto the open configuration to calculate the OSI (see [61]).

3 Mechanical aortic valve

3.1 Geometry and motion modeling

The model of the mechanical aortic valve consists of a pipe and two rotating plates inside (see Fig. 16). Three of the edges of the plates are straight, and the fourth edge is an elliptical arc. This type of valve is used widely in medical treatment, and we extracted the geometry from the pictures at [62]. Figures 17 and 18 show the plate positions and how

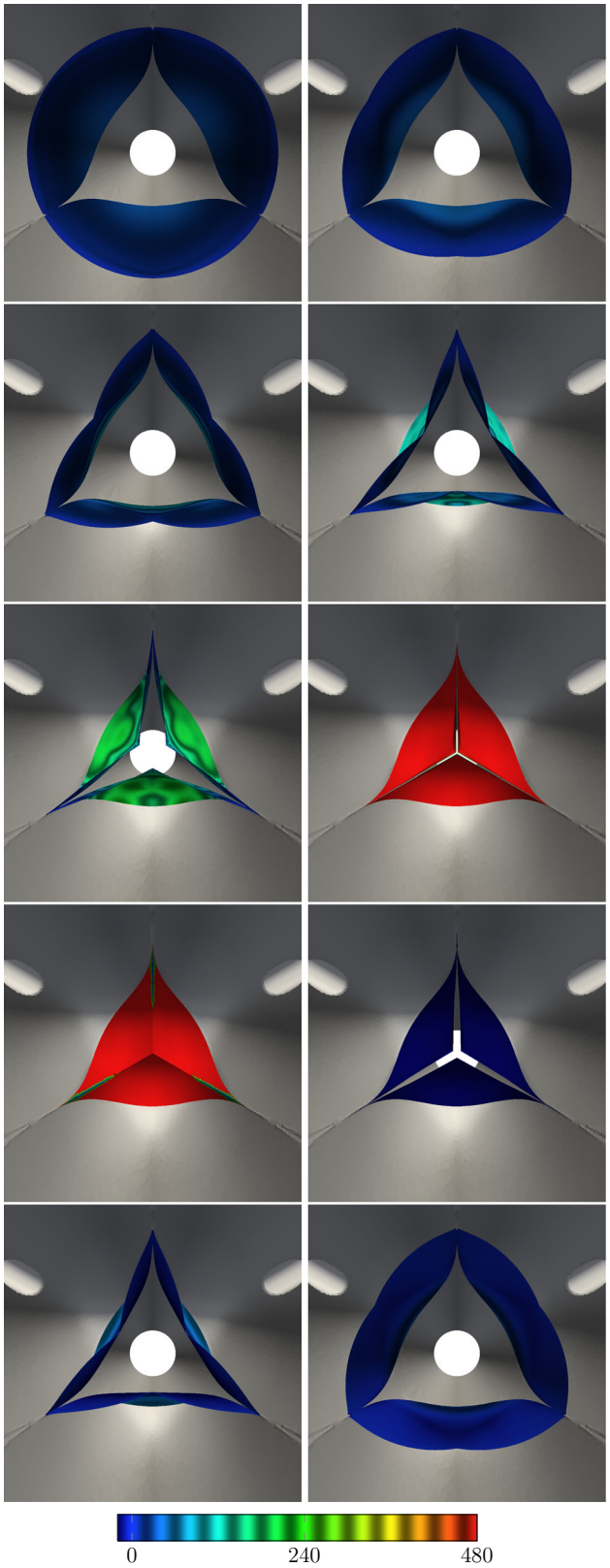

Fig. 12 Aortic valve with coronary arteries. Pressure difference (Pa) between the lower and upper surfaces of the three leaflets at the same instants as in Fig. 2

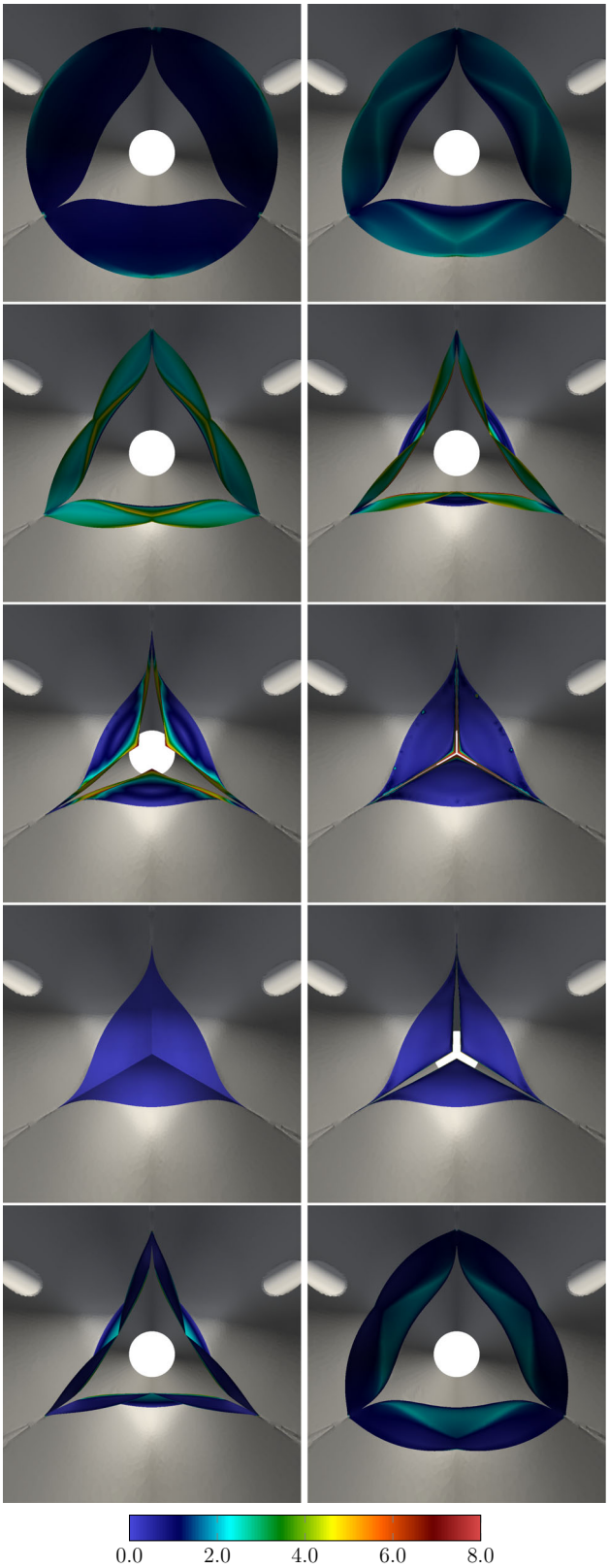

Fig. 13 Aortic valve with coronary arteries. WSS (Pa) on the lower surface of the three leaflets at the same instants as in Fig. 2

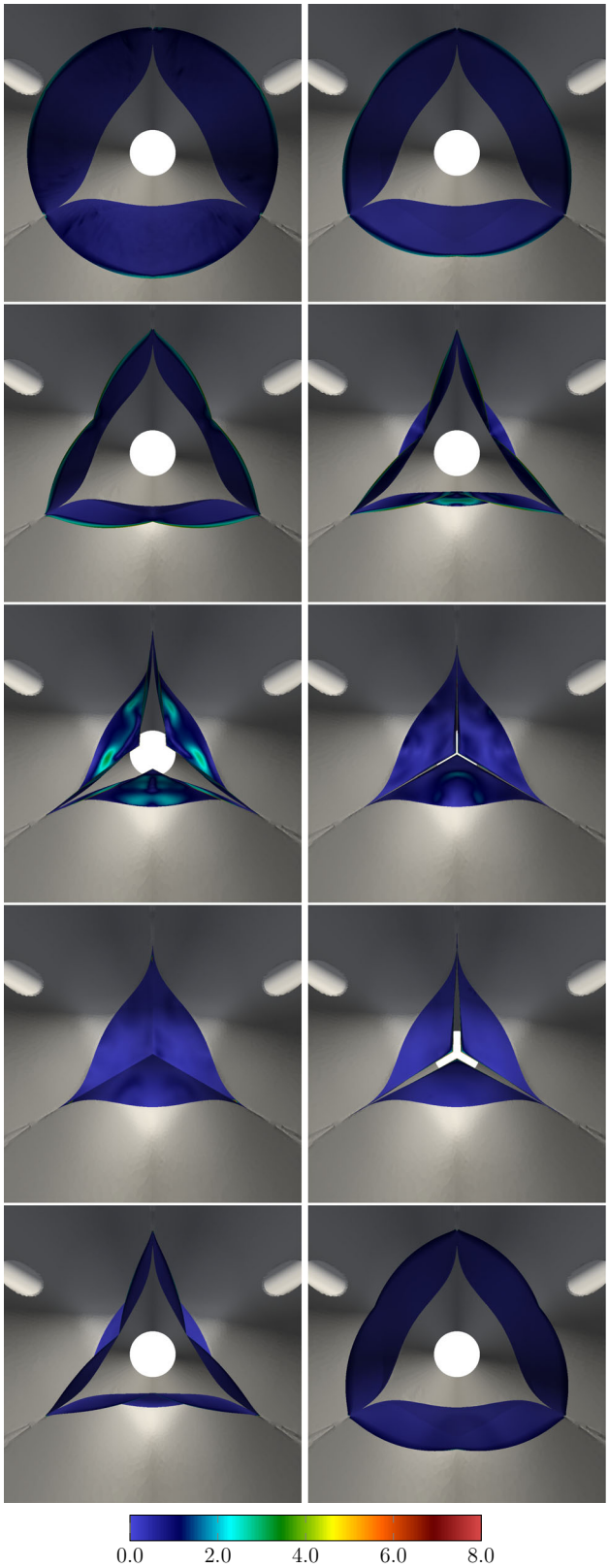

Fig. 14 Aortic valve with coronary arteries. WSS (Pa) on the upper surface of the three leaflets at the same instants as in Fig. 2

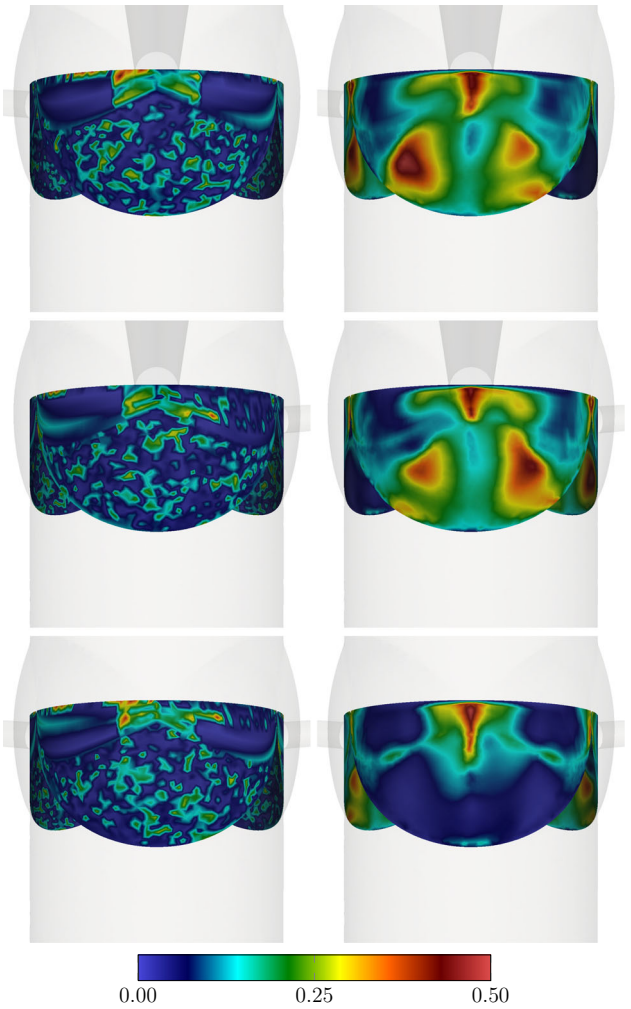

Fig. 15 Aortic valve with coronary arteries. OSI on the lower (*left*) and upper (*right*) surfaces of the leaflets. The leaflets are in the fully-open configuration, and the left, right and posterior aortic sinuses are shown in the frames from *top* to *bottom*, respectively

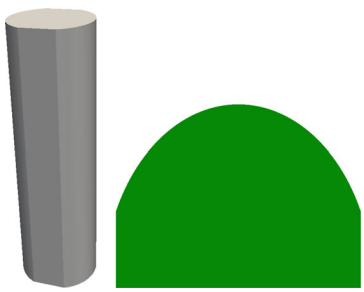

Fig. 16 Mechanical aortic valve. The pipe (*left*) and a valve plate (*right*)

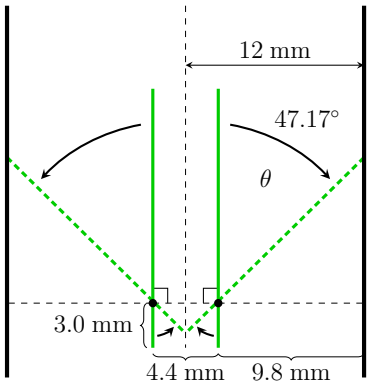

Fig. 17 Mechanical aortic valve. The plate dimensions and positions

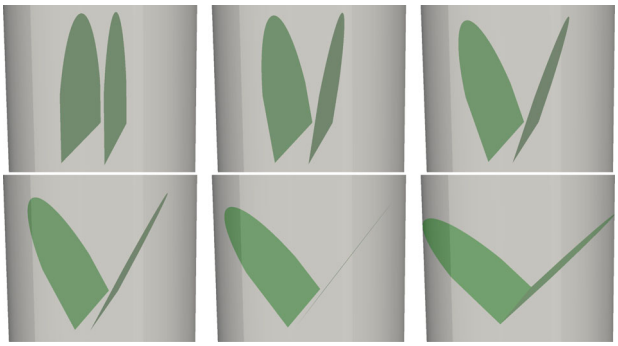

Fig. 18 Mechanical aortic valve. The plates at $\theta = 0.0°$, 9.43°, 18.87°, 28.30°, 37.73° and 47.17°

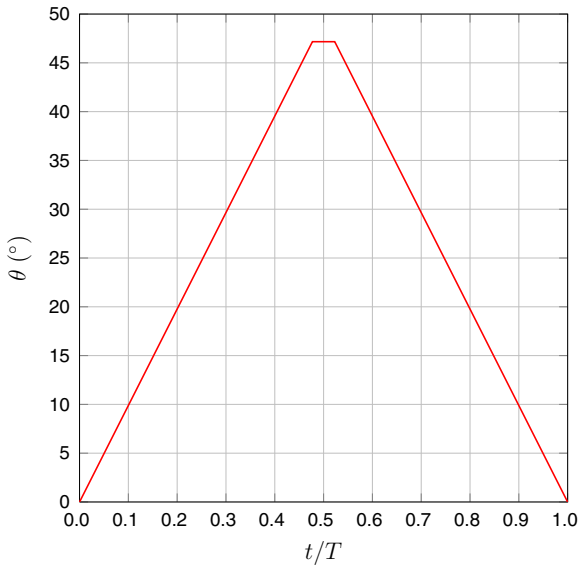

Fig. 19 Mechanical aortic valve. The rotation angle during a cycle

they rotate, with the rotation angle θ defined in Fig. 17. The flow passages between the plates and between each plate and the pipe wall are all blocked when the valve is closed at $\theta = 47.17°$. The valve closes and opens with a period of $T = 1.597$ s, and Fig. 19 shows θ during a cycle. The flow rate during a cycle is given in Fig. 20. The average flow rate is 5,736 mℓ/min. The density and kinematic viscosity of the fluid are 1,052 kg/m^3 and 4.0×10^{-6} m^2/s. The boundary conditions are no-slip on the pipe walls and plates, and uniform velocity at the inflow boundary. At the outflow

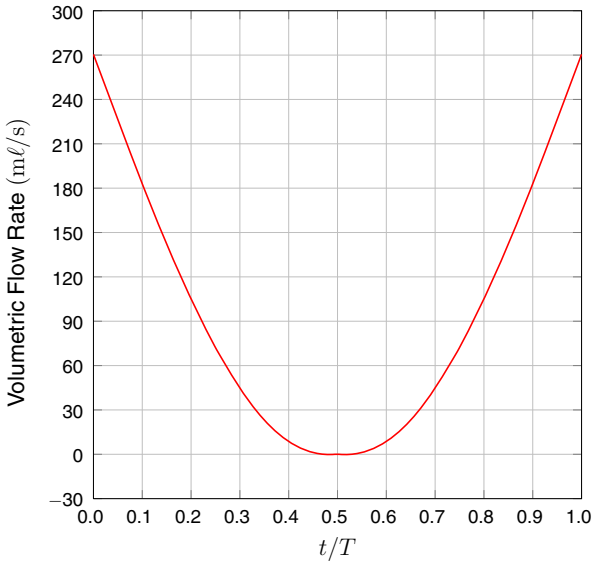

Fig. 20 Mechanical aortic valve. Inflow profile

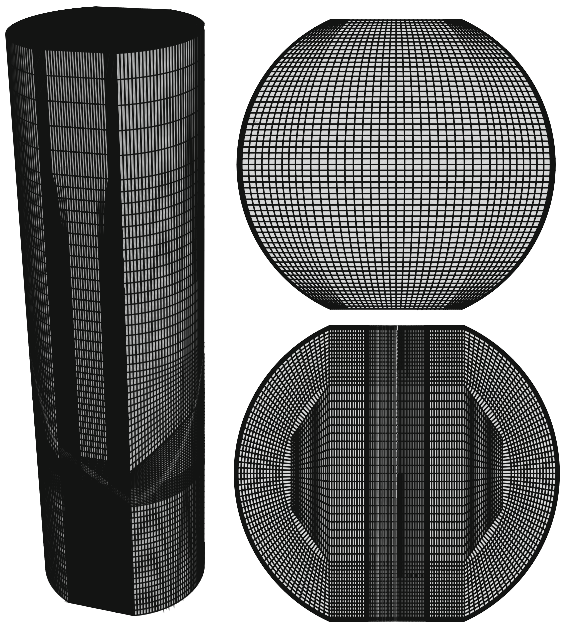

Fig. 21 Mechanical aortic valve. Surface mesh on the pipe wall (*left*) and the meshes at the outflow (*top right*) and inflow (*bottom right*) boundaries

boundary, we use the technique described in [22] to control the reverse flow.

Each surface of a plate is made of 3,444 nodes and 3,354 quadrilateral faces. The surface mesh on the pipe wall is shown in Fig. 21, together with the meshes at the inflow and outflow boundaries. The volume mesh is generated all manually and consists of 1,241,163 nodes and 1,217,264 tetrahedral, pyramid-shaped and wedge-shaped elements. Figure 22 is a schematic depiction of the block structure of the mesh when the valve is open and closed. A cross-section of the

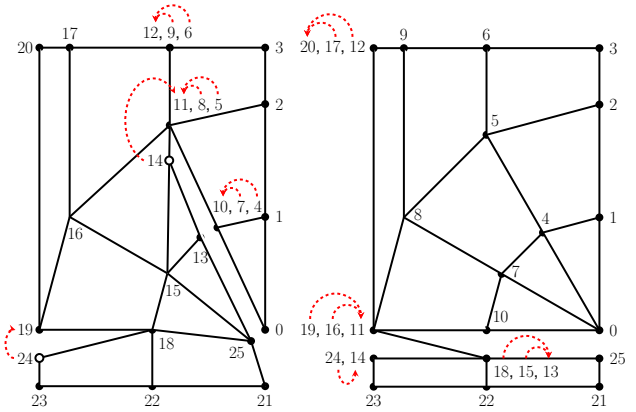

Fig. 22 Mechanical aortic valve. Block structure of the mesh near a plate when the valve is open (*left*) and closed (*right*). The small circular arcs made of *dashed lines* and *arrows* denote the nodes in master–slave relationship, with the arrow pointing to the master (see [1] for the concept of master and slave nodes in the ST-TC method). The set of nodes {25,13,14} is on the lower surface of the plate, and the set {0,10,11} the upper surface. When the valve is open, node 14 is a slave of node 11, representing the top edge of the plate. When the valve is closed, node 14 is a master and node 24 is its slave. At the same time, node 19 is a slave of node 11. With this nodal master–slave design, the domain is completely separated into the upper and lower parts when the valve is closed. The other nodes in the figure are for maintaining layers of refined mesh near the plate surfaces so that we have a more accurate representation of the boundary layers, and for having somewhat uniform mesh in the outflow-boundary region

actual volume mesh at different values of θ is shown in Figs. 23 and 24.

3.2 Computational conditions

We use the DSD/SST-VMST (convective) technique. The stabilization parameter τ_{SUPS} comes from the τ_{SUPG} definition in [2], specifically the definition given by Eqs. (107)–(109) in [2], which can also be found as the definition given by Eqs. (7)–(9) in [12], with h_{RGN} $(= h_{\text{RGNT}})$ and ν_{LSIC} $(= \nu_{\text{LSIC-HRGN}})$ given by Eqs. (15) and (19) in [57]. The time-step size is 3.175×10^{-3} s. We use 3 nonlinear iterations per time step, with 600 GMRES iterations per nonlinear iteration. Prior to the prescribed valve motion, we compute 132 time steps at the fully-open configuration to develop the flow field. The viscosity of 4.0×10^{-6} m^2/s is reached by ramping over 30 time steps starting from the viscosity 4.0×10^{-4} m^2/s. The ramping profile for the viscosity is designed to result in a linear ramping for the Reynolds number. We compute two cycles and display the results for the second cycle.

3.3 Results

The global mass-balance error, normalized by the average flow rate, is less than 5%. Figures 25 and 26 show a volume rendering of the velocity magnitude. We see mostly symmet-

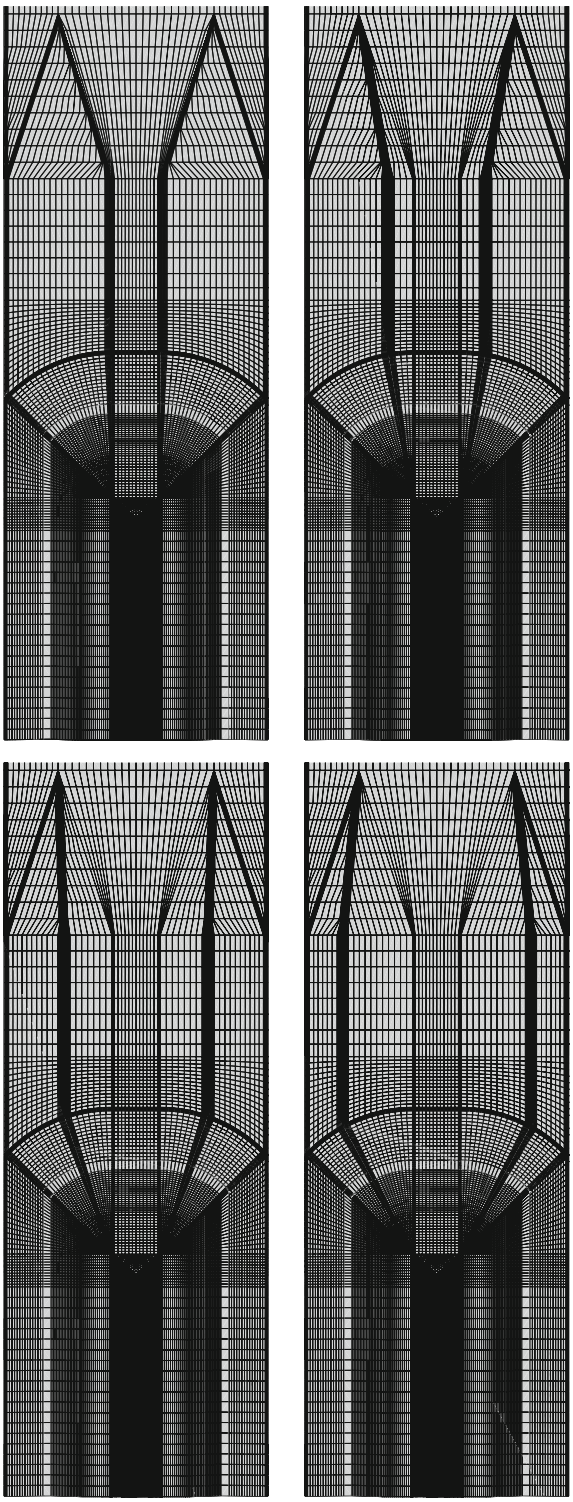

Fig. 23 Mechanical aortic valve. A cross-section of the mesh at $\theta = 0.0°$, 9.43°, 18.87° and 28.30°

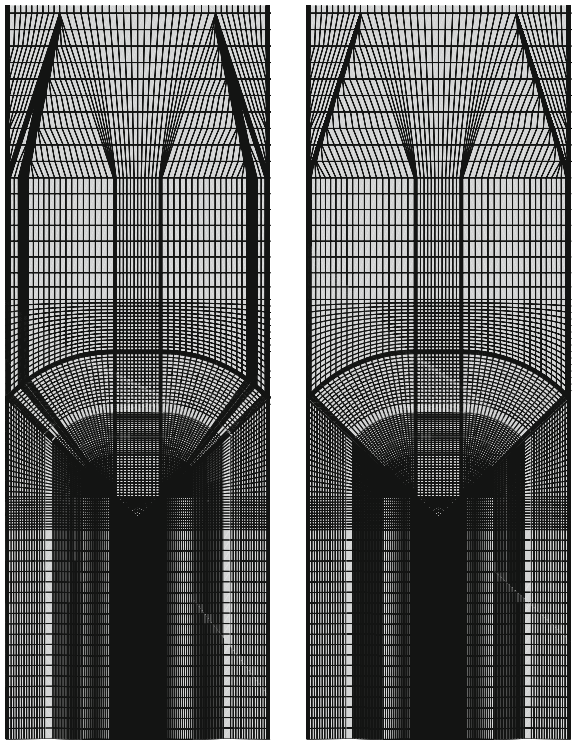

Fig. 24 Mechanical aortic valve. The cross-section of the mesh shown in Fig. 23 at $\theta = 37.73°$ and 47.17°

ric flow patterns around the valve, nonsymmetric patterns in the flow passage between the plates because of the jet there (see the picture corresponding to $t/T = 0.8$), and nonsymmetric patterns downstream. The jet fluctuates left and right, and in the picture corresponding to $t/T = 0.8$ the jet is bent to the right. Figures 27 and 28 show the WSS vectors on the upper and lower surfaces of a plate, viewed in a direction normal to the plate surface. The upper surface, which is most of the time sheltered from the inflow, has in general lower WSS, with high values only when $\theta = 0.0°$. Near the curved edge of the plate, sometimes we see the WSS vector having negative component in the inflow direction. The lower surface, which is most of the time not sheltered from the inflow, has higher WSS, and the WSS vector always has positive component in the flow direction. Figure 29 shows the moment acting on each plate with respect to its rotation center. We note that when the valve is completely closed, because the lower domain is not connected to the upper one, the pressure is determinable up to an arbitrary constant in the lower domain. However, the computation maintains the pressure to be comparable to what it was before the valve was closed, and this can be seen in the figure.

4 Concluding remarks

We have extended the ST-TC method to 3D fluid mechanics computation of heart valve models. The ST-TC method, which is an interface-tracking method, can deal with an actual

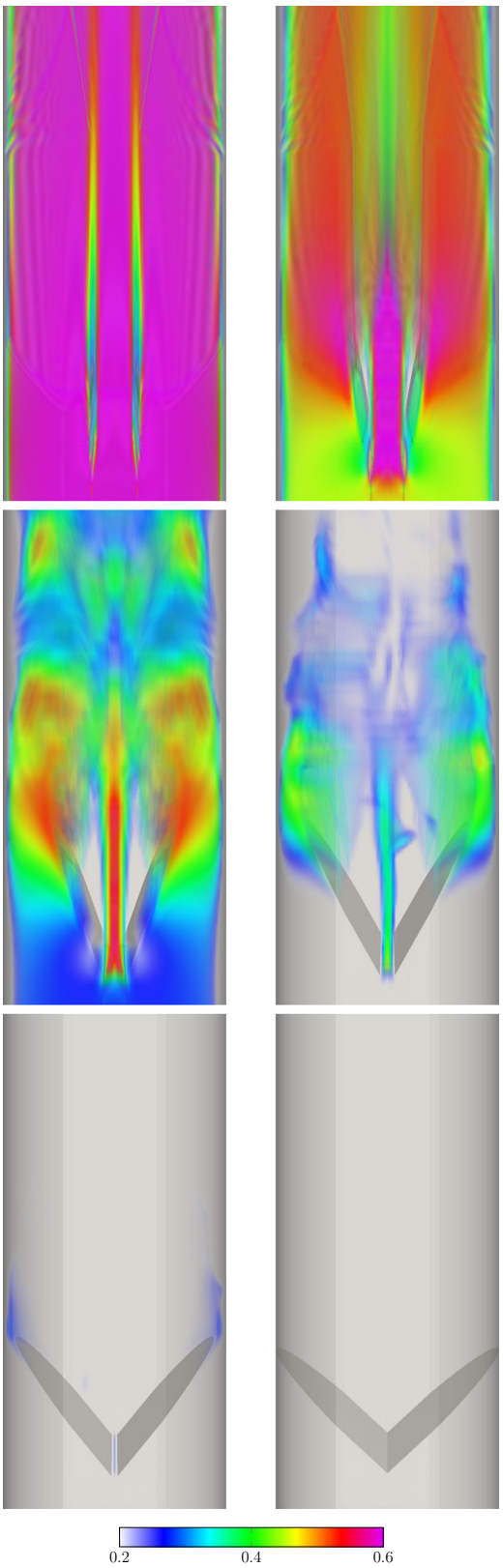

Fig. 25 Mechanical aortic valve. Volume rendering of the velocity magnitude (m/s) at $t/T = 0.0$, 0.1, 0.2, 0.3, 0.4 and 0.5

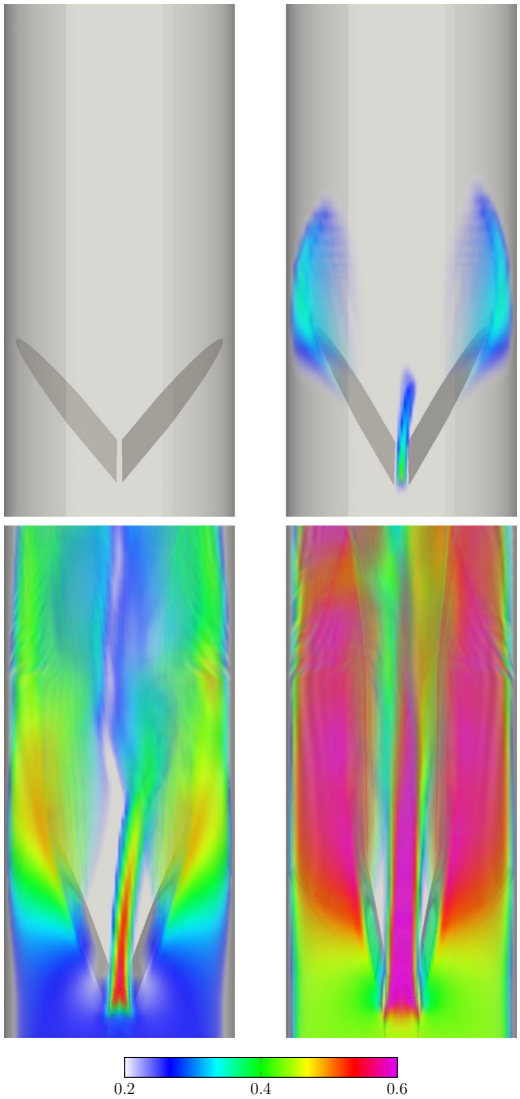

Fig. 26 Mechanical aortic valve. Volume rendering of the velocity magnitude (m/s) at $t/T = 0.6$, 0.7, 0.8 and 0.9

contact between solid surfaces in flow problems with moving interfaces, while still possessing the desirable features of interface-tracking methods, such as better resolution of the boundary layers. The ST-TC method is a new version of the DSD/SST method, and the DSD/SST method can already handle moving-interface problems when the solid surfaces are in near contact or create near TC, if the "nearness" is sufficiently "near" for the purpose of solving the problem. By not giving up on interface-tracking accuracy even where there is an actual contact between solid surfaces or other TC, the ST-TC method enables accurate representation of the flow between the heart valve surfaces even just before they close. In fact, fluid mechanics computation of heart valves with an interface-tracking method was one of the classes of compu-

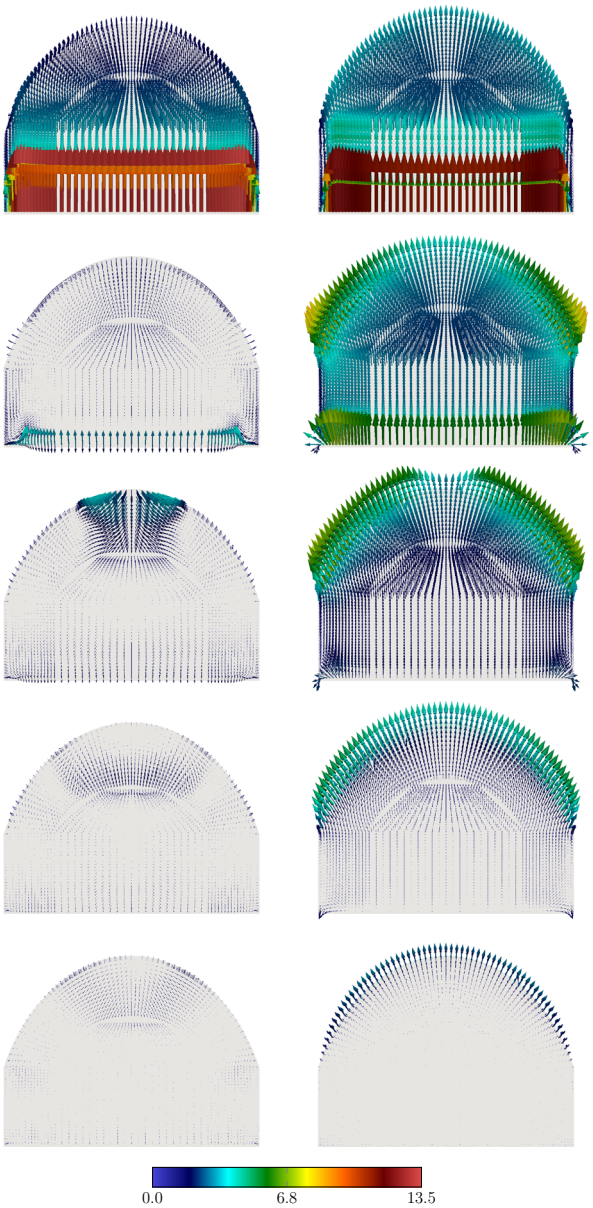

Fig. 27 Mechanical aortic valve. WSS vectors on the upper (*left*) and lower (*right*) surfaces of the plate at $t/T = 0.0$, 0.1, 0.2, 0.3 and 0.4. The *color scale* is in Pa

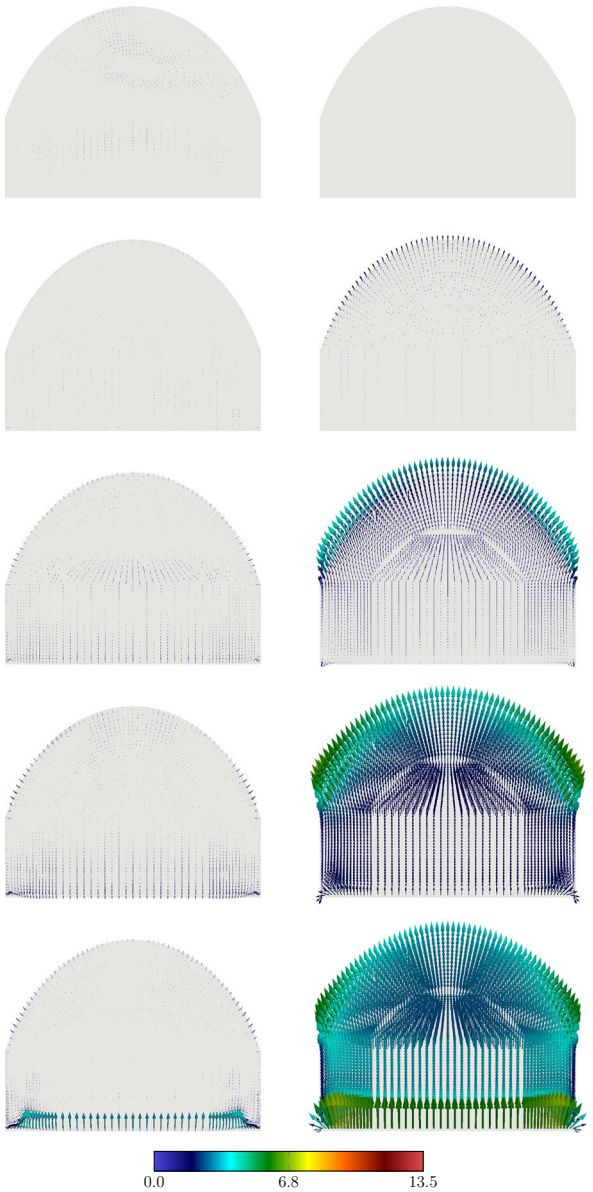

Fig. 28 Mechanical aortic valve. WSS vectors on the upper (*left*) and lower (*right*) surfaces of the plate at $t/T = 0.5$, 0.6, 0.7, 0.8 and 0.9. The *color scale* is in Pa

tations targeted in introducing the ST-TC method. This paper is essentially a continuation of the paper [1] where the ST-TC method was introduced and 2D test computations with models representative of the classes of problems targeted with the method were presented. Here we have presented 3D computations for two heart valve models: an aortic valve with coronary arteries and a mechanical aortic valve. These computations show that the ST-TC method can bring interface-tracking accuracy to fluid mechanics of heart valves, and can do that with computational practicality.

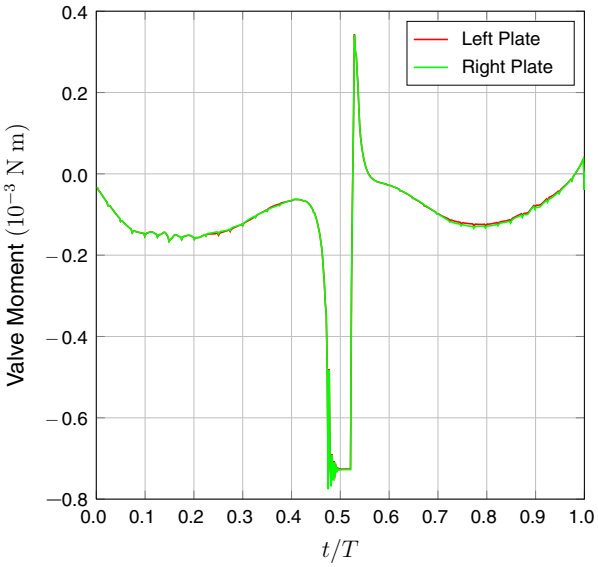

Fig. 29 Mechanical aortic valve. The moment acting on each plate with respect to its rotation center. Positive moment increases θ

Acknowledgments This work was supported in part by JST-CREST and Rice–Waseda research agreement (first and fourth authors).

References

1. Takizawa K, Tezduyar TE, Buscher A, Asada, S (October 2013) Space–time interface-tracking with topology change (ST-TC). Comput Mech. doi:10.1007/s00466-013-0935-7
2. Tezduyar TE (2003) Computation of moving boundaries and interfaces and stabilization parameters. Int J Numer Methods Fluids 43:555–575. doi:10.1002/fld.505
3. Tezduyar TE, Sathe S, Pausewang J, Schwaab M, Christopher J, Crabtree J (2008) Interface projection techniques for fluid–structure interaction modeling with moving-mesh methods. Comput Mech 43:39–49. doi:10.1007/s00466-008-0261-7
4. Bazilevs Y, Takizawa K, Tezduyar TE (2013) Computational fluid–structure interaction: methods and applications. Wiley, London. ISBN:978-0470978771
5. Takizawa K, Bazilevs Y, Tezduyar TE (2012) Space–time and ALE-VMS techniques for patient-specific cardiovascular fluid–structure interaction modeling. Arch Comput Methods Eng 19:171–225. doi:10.1007/s11831-012-9071-3
6. Takizawa K, Schjodt K, Puntel A, Kostov N, Tezduyar TE (2012) Patient-specific computer modeling of blood flow in cerebral arteries with aneurysm and stent. Comput Mech 50:675–686. doi:10.1007/s00466-012-0760-4
7. Takizawa K, Schjodt K, Puntel A, Kostov N, Tezduyar TE (2013) Patient-specific computational analysis of the influence of a stent on the unsteady flow in cerebral aneurysms. Comput Mech 51:1061–1073. doi:10.1007/s00466-012-0790-y
8. Takizawa K, Bazilevs Y, Tezduyar TE, Long CC, Marsden AL, Schjodt K (2014) ST and ALE-VMS methods for patient-specific cardiovascular fluid mechanics modeling. Math Models Methods Appl Sci. doi:10.1142/S0218202514500250
9. Tezduyar TE (1992) Stabilized finite element formulations for incompressible flow computations. Adv Appl Mech 28:1–44. doi:10.1016/S0065-2156(08)70153-4
10. Tezduyar TE, Behr M, Liou J (1992) A new strategy for finite element computations involving moving boundaries and interfaces—the deforming-spatial-domain/space–time procedure: I. The concept and the preliminary numerical tests. Comput Methods Appl Mech Eng 94:339–351. doi:10.1016/0045-7825(92)90059-S
11. Tezduyar TE, Behr M, Mittal S, Liou J (1992) A new strategy for finite element computations involving moving boundaries and interfaces—the deforming-spatial-domain/space–time procedure: II. Computation of free-surface flows, two-liquid flows, and flows with drifting cylinders. Comput Methods Appl Mech Eng 94:353–371. doi:10.1016/0045-7825(92)90060-W
12. Tezduyar TE, Sathe S (2007) Modeling of fluid–structure interactions with the space–time finite elements: solution techniques. Int J Numer Methods Fluids 54:855–900. doi:10.1002/fld.1430
13. Takizawa K, Tezduyar TE (2011) Multiscale space–time fluid–structure interaction techniques. Comput Mech 48:247–267. doi:10.1007/s00466-011-0571-z
14. Takizawa K, Tezduyar TE (2012) Space–time fluid–structure interaction methods. Math Models Methods Appl Sci 22:1230001. doi:10.1142/S0218202512300013
15. Hughes TJR, Liu WK, Zimmermann TK (1981) Lagrangian–Eulerian finite element formulation for incompressible viscous flows. Comput Methods Appl Mech Eng 29:329–349
16. Ohayon R (2001) Reduced symmetric models for modal analysis of internal structural-acoustic and hydroelastic-sloshing systems. Comput Methods Appl Mech Eng 190:3009–3019
17. van Brummelen EH, de Borst R (2005) On the nonnormality of subiteration for a fluid–structure interaction problem. SIAM J Sci Comput 27:599–621
18. Bazilevs Y, Calo VM, Zhang Y, Hughes TJR (2006) Isogeometric fluid–structure interaction analysis with applications to arterial blood flow. Comput Mech 38:310–322
19. Khurram RA, Masud A (2006) A multiscale/stabilized formulation of the incompressible Navier–Stokes equations for moving boundary flows and fluid–structure interaction. Comput Mech 38:403–416
20. Bazilevs Y, Calo VM, Hughes TJR, Zhang Y (2008) Isogeometric fluid–structure interaction: theory, algorithms, and computations. Comput Mech 43:3–37
21. Dettmer WG, Peric D (2008) On the coupling between fluid flow and mesh motion in the modelling of fluid–structure interaction. Comput Mech 43:81–90
22. Bazilevs Y, Gohean JR, Hughes TJR, Moser RD, Zhang Y (2009) Patient-specific isogeometric fluid–structure interaction analysis of thoracic aortic blood flow due to implantation of the Jarvik 2000 left ventricular assist device. Comput Methods Appl Mech Eng 198:3534–3550
23. Bazilevs Y, Hsu M-C, Benson D, Sankaran S, Marsden A (2009) Computational fluid–structure interaction: methods and application to a total cavopulmonary connection. Comput Mech 45:77–89
24. Bazilevs Y, Hsu M-C, Zhang Y, Wang W, Liang X, Kvamsdal T, Brekken R, Isaksen J (2010) A fully-coupled fluid–structure interaction simulation of cerebral aneurysms. Comput Mech 46:3–16
25. Bazilevs Y, Hsu M-C, Zhang Y, Wang W, Kvamsdal T, Hentschel S, Isaksen J (2010) Computational fluid–structure interaction: methods and application to cerebral aneurysms. Biomech Model Mechanobiol 9:481–498
26. Bazilevs Y, Hsu M-C, Akkerman I, Wright S, Takizawa K, Henicke B, Spielman T, Tezduyar TE (2011) 3D simulation of wind turbine rotors at full scale. Part I: Geometry modeling and aerodynamics. Int J Numer Methods Fluids 65:207–235. doi:10.1002/fld.2400
27. Bazilevs Y, Hsu M-C, Kiendl J, Wüchner R, Bletzinger K-U (2011) 3D simulation of wind turbine rotors at full scale. Part II: Fluid–structure interaction modeling with composite blades. Int J Numer Methods Fluids 65:236–253

28. Akkerman I, Bazilevs Y, Kees CE, Farthing MW (2011) Isogeometric analysis of free-surface flow. J Comput Phys 230:4137–4152
29. Hsu M-C, Bazilevs Y (2011) Blood vessel tissue prestress modeling for vascular fluid–structure interaction simulations. Finite Elem Anal Des 47:593–599
30. Nagaoka S, Nakabayashi Y, Yagawa G, Kim YJ (2011) Accurate fluid–structure interaction computations using elements without mid-side nodes. Comput Mech 48:269–276. doi:10.1007/s00466-011-0620-7
31. Bazilevs Y, Hsu M-C, Takizawa K, Tezduyar TE (2012) ALE-VMS and ST-VMS methods for computer modeling of wind-turbine rotor aerodynamics and fluid–structure interaction. Math Models Methods Appl Sci 22:1230002. doi:10.1142/S0218202512300025
32. Akkerman I, Bazilevs Y, Benson DJ, Farthing MW, Kees CE (2012) Free-surface flow and fluid-object interaction modeling with emphasis on ship hydrodynamics. J Appl Mech 79:010905
33. Bazilevs Y, Hsu M-C, Scott MA (2012) Isogeometric fluid–structure interaction analysis with emphasis on non-matching discretizations, and with application to wind turbines. Comput Methods Appl Mech Eng 249–252:28–41
34. Hsu M-C, Akkerman I, Bazilevs Y (2012) Wind turbine aerodynamics using ALE-VMS: validation and role of weakly enforced boundary conditions. Comput Mech 50:499–511
35. Hsu M-C, Bazilevs Y (2012) Fluid–structure interaction modeling of wind turbines: simulating the full machine. Comput Mech 50:821–833
36. Akkerman I, Dunaway J, Kvandal J, Spinks J, Bazilevs Y (2012) Toward free-surface modeling of planing vessels: simulation of the Fridsma hull using ALE-VMS. Comput Mech 50:719–727
37. Minami S, Kawai H, Yoshimura S (2012) Parallel BDD-based monolithic approach for acoustic fluid–structure interaction. Comput Mech 50:707–718
38. Miras T, Schotte J-S, Ohayon R (2012) Energy approach for static and linearized dynamic studies of elastic structures containing incompressible liquids with capillarity: a theoretical formulation. Comput Mech 50:729–741
39. van Opstal TM, van Brummelen EH, de Borst R, Lewis MR (2012) A finite-element/boundary-element method for large-displacement fluid–structure interaction. Comput Mech 50:779–788
40. Yao JY, Liu GR, Narmoneva DA, Hinton RB, Zhang Z-Q (2012) Immersed smoothed finite element method for fluid–structure interaction simulation of aortic valves. Comput Mech 50:789–804
41. Larese A, Rossi R, Onate E, Idelsohn SR (2012) A coupled PFEM-Eulerian approach for the solution of porous FSI problems. Comput Mech 50:805–819
42. Bazilevs Y, Takizawa K, Tezduyar TE (2013) Challenges and directions in computational fluid–structure interaction. Math Models Methods Appl Sci 23:215–221. doi:10.1142/S0218202513400010
43. Bazilevs Y, Hsu M-C, Bement MT (2013) Adjoint-based control of fluid–structure interaction for computational steering applications. Procedia Comput Sci 18:1989–1998
44. Korobenko A, Hsu M-C, Akkerman I, Tippmann J, Bazilevs Y (2013) Structural mechanics modeling and FSI simulation of wind turbines. Math Models Methods Appl Sci 23:249–272
45. Korobenko A, Hsu M-C, Akkerman I, Bazilevs Y (2013) Aerodynamic simulation of vertical-axis wind turbines. J Appl Mech 81:021011. doi:10.1115/1.4024415
46. Bazilevs Y, Korobenko A, Deng X, Yan J, Kinzel M, Dabiri JO (2014) FSI modeling of vertical-axis wind turbines. J Appl Mech. doi:10.1115/1.4027466
47. Yao JY, Liu GR, Qian D, Chen CL, Xu GX (2013) A moving-mesh gradient smoothing method for compressible CFD problems. Math Models Methods Appl Sci 23:273–305
48. Kamran K, Rossi R, Onate E, Idelsohn SR (2013) A compressible Lagrangian framework for modeling the fluid–structure interaction in the underwater implosion of an aluminum cylinder. Math Models Methods Appl Sci 23:339–367
49. Hsu M-C, Akkerman I, Bazilevs Y (2014) Finite element simulation of wind turbine aerodynamics: validation study using NREL Phase VI experiment. Wind Energy 17:461–481
50. Long CC, Marsden AL, Bazilevs Y (2013) Fluid–structure interaction simulation of pulsatile ventricular assist devices. Comput Mech 52:971–981. doi:10.1007/s00466-013-0858-3
51. Long CC, Esmaily-Moghadam M, Marsden AL, Bazilevs Y (2013) Computation of residence time in the simulation of pulsatile ventricular assist devices. Comput Mech. doi:10.1007/s00466-013-0931-y
52. Yao J, Liu GR (2014) A matrix-form GSM-CFD solver for incompressible fluids and its application to hemodynamics. Comput Mech. doi:10.1007/s00466-014-0990-8
53. Long CC, Marsden AL, Bazilevs Y (2014) Shape optimization of pulsatile ventricular assist devices using FSI to minimize thrombotic risk. Comput Mech. doi:10.1007/s00466-013-0967-z
54. Takizawa K, Henicke B, Puntel A, Spielman T, Tezduyar TE (2012) Space–time computational techniques for the aerodynamics of flapping wings. J Appl Mech 79:010903. doi:10.1115/1.4005073
55. Takizawa K, Henicke B, Puntel A, Kostov N, Tezduyar TE (2012) Space–time techniques for computational aerodynamics modeling of flapping wings of an actual locust. Comput Mech 50:743–760. doi:10.1007/s00466-012-0759-x
56. Takizawa K, Kostov N, Puntel A, Henicke B, Tezduyar TE (2012) Space–time computational analysis of bio-inspired flapping-wing aerodynamics of a micro aerial vehicle. Comput Mech 50:761–778. doi:10.1007/s00466-012-0758-y
57. Takizawa K, Tezduyar TE, McIntyre S, Kostov N, Kolesar R, Habluetzel C (2014) Space–time VMS computation of wind-turbine rotor and tower aerodynamics. Comput Mech 53:1–15. doi:10.1007/s00466-013-0888-x
58. Takizawa K, Tezduyar TE, Kostov N (2014) Sequentially-coupled space–time FSI analysis of bio-inspired flapping-wing aerodynamics of an MAV. Comput Mech. doi:10.1007/s00466-014-0980-x
59. Tezduyar TE, Takizawa K, Moorman C, Wright S, Christopher J (2010) Space–time finite element computation of complex fluid–structure interactions. Int J Numer Methods Fluids 64:1201–1218. doi:10.1002/fld.2221
60. Griffith BE, Luo X, McQueen DM, Peskin CS (2009) Simulating the fluid dynamics of natural and prosthetic heart valves using the immersed boundary method. Int J Appl Mech 1:137–177
61. Takizawa K, Moorman C, Wright S, Christopher J, Tezduyar TE (2010) Wall shear stress calculations in space–time finite element computation of arterial fluid–structure interactions. Comput Mech 46:31–41. doi:10.1007/s00466-009-0425-0
62. On-X Life Technologies, Inc.—designed for life. http://www.onxlti.com/